International Journal
of Micro Air Vehicles

ORIGINAL RESEARCH ARTICLE

Open Access

https://doi.org/10.48130/mav-0026-0004

International Journal of Micro Air Vehicles **2026**, 18: e005

A cooperative obstacle avoidance control scheme for multi-quadrotor UAV formation: a hierarchical control approach

Zhipeng Liu[1,2], Fuyuan Xie[1,2] and Xiangyu Wang[1,2,3*]

[1] *School of Automation, Southeast University, Nanjing 210096, China*
[2] *Key Laboratory of Measurement and Control of Complex Systems of Engineering, Ministry of Education, Nanjing 210096, China*
[3] *School of Future Technology, Southeast University, Nanjing 211189, China*
* Correspondence: w.x.y@seu.edu.cn (Wang X)

Abstract

In this work, a hierarchical distributed control scheme is proposed to address the cooperative formation and obstacle avoidance problem faced during the application of multi-quadrotor unmanned aerial vehicle (UAV) systems. The distributed control design is decoupled into a two-layer structure consisting of an upper layer for reference signal generation and a lower layer for tracking control. In the upper layer, an adaptive repulsive gain mechanism is introduced into the repulsive force. Based on the adaptive artificial potential field (AAPF) method, an obstacle avoidance trajectory is generated for the virtual leader and it is incorporated into a distributed reference signal generator, which subsequently produces the required reference signals for UAV formation obstacle avoidance. In the lower layer, tracking controllers integrated with an extended state observer (ESO) are designed for multi-quadrotor UAVs. Lyapunov-based stability analysis demonstrates the exponential convergence of the upper-layer error signals and the boundedness of the lower-layer error signals. Finally, the experimental results validate the effectiveness of the proposed control scheme.

Keywords: Multi-quadrotor UAVs, Formation control, Obstacle avoidance, Artificial potential field, Hierarchical design

Citation: Liu Z, Xie F, Wang X. 2026. A cooperative obstacle avoidance control scheme for multi-quadrotor UAV formation: a hierarchical control approach. *International Journal of Micro Air Vehicles* 18: e005 https://doi.org/10.48130/mav-0026-0004

Introduction

Multi-quadrotor unmanned aerial vehicles (UAVs) are defined by their multirotor actuation features and multiple degrees of freedom, which enable flexible trajectory tracking and agile attitude adjustment[1−3]. These capabilities make multi-quadrotor UAVs well suited for cooperative missions. Using cooperative control algorithms, multi-quadrotor UAV systems can accomplish swarm tasks, supporting applications such as load transportation[4], target surveillance[5], and search and strike[6]. When obstacle-free scenarios are considered, formation control can be addressed effectively. However, in practical mission scenarios, the spatial constraints imposed by complex three-dimensional (3D) obstacle environments tightly couple formation maintenance with obstacle avoidance. This poses challenges for conventional cooperative control algorithms in achieving both objectives simultaneously.

The main formation control strategies include virtual structure methods[7−9], behavior-based methods[10−12], and consensus algorithms[13−15]. Belkacem et al.[16] developed a distributed algorithm for achieving consensus tracking in second-order multiagent systems that avoids the chattering effect typically induced by traditional sliding-mode control protocols. Zhang et al.[17] framed a leader–follower cooperative guidance law via backstepping approach based on graph theoretic communication topology. Ollervides-Vazquez et al.[18] developed a sectorial fuzzy consensus approach for the formation flight of multi-quadrotor UAVs based on the Newton–Euler model and a sectorial fuzzy controller. Miao et al.[19] introduced a distributed formation control scheme that operates without requiring outer-loop linear velocity or inner-loop angular velocity measurements. In distributed formation control, individual coordination is strongly linked to collective behavior, with heavy reliance on cooperative error feedback and accurate system models. This reliance reduces flexibility and substantially complicates controller design as system complexity increases. Moreover, multifunctionality and scalability are often constrained by packaging limitations. Accordingly, Wang et al.[20] presented a hierarchical distributed control framework that decouples the problem into a reference generation layer and a tracking control layer. Furthermore, Wang et al.[21] investigated the consensus problem of second-order leader–follower systems with velocity constraints and developed a hierarchical constrained distributed control scheme.

Unknown obstacles in practical mission scenarios pose a critical challenge to the safety of cooperative formations. Consequently, various approaches have been proposed for obstacle avoidance, including graph search algorithms[22], genetic algorithms[23], and reinforcement learning methods[24]. Compared with the aforementioned methods, the artificial potential field (APF) method guides the agent by superimposing an attractive potential toward the goal and a repulsive potential away from obstacles, thereby generating an obstacle avoidance trajectory from the start to the goal[25]. As the APF method features structural simplicity, real-time implementability, and rapid responsiveness to environmental changes, it has been widely applied to collision avoidance[26−28] and obstacle avoidance[29−31]. Matoui et al.[32] developed a centralized APF-based planner to generate trajectories for multirobot systems that operate in dynamic environments. Hu et al.[33] reported an integrated approach that combines Voronoi partitions with a conventional APF to achieve distributed formation control and collision avoidance. To mitigate the inherent local minima and oscillatory behavior of conventional APF methods, Pan et al.[34] developed a hybrid formation control scheme by combining a rotational potential field with a leader–follower strategy, enabling follower UAVs to maintain prescribed relative angles and distances with respect to the leader. Huang et al.[35] introduced a parallel search strategy to mitigate the

© The Author(s)

https://doi.org/10.48130/mav-0026-0004

local minimum trap and goal inaccessibility problems that arise near obstacles in conventional APF methods. For dynamic obstacle avoidance, Wang et al.[36] modified the repulsive potential function and introduced an adaptive repulsion coefficient that depends on the obstacle velocity. Furthermore, Liu et al.[37] developed an improved repulsive force with a continuously differentiable regulation mechanism, which eliminates the influence of obstacles outside the detection range. Despite the proven feasibility of existing formation obstacle avoidance methods, the limited flexibility of traditional distributed control frameworks poses a challenge.

Inspired by the aforementioned research, this paper proposes a hierarchical distributed formation obstacle avoidance control scheme for multi-quadrotor UAVs in 3D obstacle environments. The proposed design consists of three steps. First, to cope with the increased collision risks induced by 3D obstacles during formation maneuvering, the formation is enclosed by a virtual sphere whose center is the virtual leader, and an adaptive artificial potential field (AAPF)-based planner is used to generate an obstacle avoidance trajectory for this sphere so that the entire formation can pass through cluttered spaces safely. Second, a distributed reference signal generator is designed to maintain the desired formation configuration and produce obstacle avoidance reference trajectories for the multi-quadrotor UAVs by embedding the virtual leader's planned trajectory. Finally, the generator outputs are taken as the reference trajectories for each multi-quadrotor UAV, and extended state observer (ESO)-based composite controllers are designed to achieve trajectory tracking under conditions of disturbances and uncertainties. The main contributions of this paper are twofold:

1. By incorporating an adaptive gain mechanism into the repulsive force, the proposed AAPF method alleviates oscillations near the obstacle avoidance boundary that commonly arise in traditional APF schemes. This design reduces sensitivity to gain tuning and enhances adaptability across different scenarios.

2. The proposed control scheme decouples the traditional distributed formation obstacle avoidance problem into a two layer structure, based on the virtual leader's obstacle avoidance trajectory planned by the AAPF method. This hierarchical framework improves the flexibility and robustness of the system design.

The rest of this paper is organized as follows. Section “Preliminaries and problem formulation” provides the preliminaries and formulates the problem. Section “Main Results” develops a hierarchical distributed formation obstacle avoidance control scheme for multi-quadrotor UAV systems. Section “Experiments” reports experimental validations and discusses the results. Finally, some conclusions are drawn in Section “Conclusions”.

Preliminaries and problem formulation

Notations: $\mathbb{R}^n$ denotes the set of n-dimensional real vectors, and $\mathbb{R}^{n\times m}$ denotes the set of $n\times m$ real matrices. Let $\mathbf{0}_m=[0,\ldots,0]^T\in\mathbb{R}^m$ and $\mathbf{0}_{n\times m}\in\mathbb{R}^{n\times m}$ be the zero vector and the zero matrix, respectively. $I_n\in\mathbb{R}^{n\times n}$ denotes the $n\times n$ identity matrix. For a symmetric matrix $A\in\mathbb{R}^{n\times n}$, $\lambda_{\min}(A)$ and $\lambda_{\max}(A)$ denote its smallest and largest eigenvalues, respectively. The Euclidean norm of a vector is denoted by $\|\cdot\|_2$. A basic property of the Rayleigh quotient is that, for any symmetric matrix $\boldsymbol{P}\in\mathbb{R}^{n\times n}$ and nonzero vector $\boldsymbol{x}\in\mathbb{R}^n$, $\lambda_{\min}(\boldsymbol{P})\|\boldsymbol{x}\|_2^2\le\boldsymbol{x}^T\boldsymbol{P}\boldsymbol{x}\le\lambda_{\max}(\boldsymbol{P})\|\boldsymbol{x}\|_2^2$.

Graph theory notions

For the leader–follower case, node 0 represents the leader, whereas nodes $1,\ldots,N$ represent the followers. The communication topology among the followers is described by an undirected graph $G=(\mathcal{V},\mathcal{E},\mathcal{A})$, where $\mathcal{V}=\{1,\ldots,N\}$ is the node set, $\mathcal{E}\subseteq\mathcal{V}\times\mathcal{V}$ is the edge set, and $\mathcal{A}=[a_{ij}]\in\mathbb{R}^{N\times N}$ is the weighted adjacency matrix with $a_{ij}=a_{ji}>0$ if $(j,i)\in\mathcal{E}$, whereas $a_{ij}=0$ otherwise, and $a_{ii}=0,\forall i\in\mathcal{V}$. The neighbor set of node i is $\mathcal{N}_i=\{j\in\mathcal{V}\mid(j,i)\in\mathcal{E}\}$. The Laplacian matrix of G is $L=[l_{ij}]\in\mathbb{R}^{N\times N}$, where $l_{ii}=\sum_{j\in\mathcal{N}_i}a_{ij}$ and $l_{ij}=-a_{ij}$ for $i\ne j$. An undirected graph is connected if there is a path between each node pair. The overall graph including the leader and followers is denoted by a directed graph $\bar{G}$ with the node set $\bar{\mathcal{V}}=\{0\}\cup\mathcal{V}$. The communication from the leader to follower i is unidirectional with an edge weight b_i, where $b_i>0$ if connected and $b_i=0$ otherwise. Define $B=\mathrm{diag}\{b_1,\ldots,b_N\}$ and $M=L+B$. A directed graph has a directed spanning tree if at least one node has paths to all other nodes.

Useful lemmas

Lemma 1. *If a directed graph $\bar{G}$ contains at least one directed spanning tree (i.e., $B\ne0$), then its graph matrix M is positive definite*[38].

Lemma 2. *Let $x,y\in\mathbb{R}$, and let $\varkappa>0$ be an arbitrary positive constant. Suppose the constants $p>1$ and $q>1$ satisfy the conjugacy condition $(p-1)(q-1)=1$. Then, xy holds $xy\le\frac{\varkappa^p}{p}|x|^p+\frac{1}{q\varkappa^q}|y|^q$*[39].

Definition 1. *Consider the system $\dot{x}=f(t,x,u)$, where $f:[0,+\infty)\times\mathbb{R}^n\times\mathbb{R}^m\to\mathbb{R}^n$ is piecewise continuous in t, and locally Lipschitz in x and u. The input $u(t)$ is a piecewise continuous, bounded function of t for all $t\ge0$. The system $\dot{x}=f(t,x,u)$ is said to be input-to-state stable (ISS) if there exist a class $\mathcal{KL}$ function $\beta(\cdot,\cdot)$ and a class $\mathcal{K}$ function $\gamma(\cdot)$ such that for any initial state $x(t_0)$ and bounded input $u(t)$, the solution $x(t)$ exists $\forall t\ge t_0$ and satisfies $\|x(t)\|_2\le\beta(\|x(t_0)\|_2,t-t_0)+\gamma\left(\sup_{t_0\le\tau\le t}\|u(\tau)\|_2\right)$*[40].

Lemma 3. *Suppose f in Definition 1 is continuously differentiable and globally Lipschitz in (x,u), uniformly in t. If the unforced system $\dot{x}=f(t,x,\mathbf{0}_m)$ is globally uniformly exponentially stable at the origin, then the system is ISS.*[40]

System modeling and problem formulation

System modeling

A team of N multi-quadrotor UAVs operating in a 3D workspace is considered. Two coordinate frames are adopted. The *inertial-reference frame* is denoted by $\mathcal{F}_{\rceil}=\{O_e,X_e,Y_e,Z_e\}$, the origin O_e is fixed at a designated point on the ground, the O_eX_e-axis can be chosen to point along an arbitrary horizontal direction, the O_eZ_e-axis is perpendicular to the ground and points upward, and the O_eY_e-axis follows the right-hand rule to complete a right-handed triad. The *body-reference frame* attached to each UAV is denoted by $\mathcal{F}_{\lfloor}=\{O_b,X_b,Y_b,Z_b\}$, the origin O_b is fixed at the UAV's center of mass, the O_bX_b-axis aligns with the body-forward direction, the O_bZ_b-axis is normal to the UAV body plane, and the O_bY_b-axis follows the right-hand rule. Each UAV generates control forces and moments by independently regulating the rotational speeds of four rotors, thereby producing a total thrust along the O_bZ_b-axis and three body torques about the O_bX_b, O_bY_b, and O_bZ_b-axes.

The communication among the multi-quadrotor UAVs is described by an undirected graph $G=(\mathcal{V},\mathcal{E},\mathcal{A})$, where $\mathcal{V}=\{1,\ldots,N\}$ is the set of follower UAVs, $\mathcal{E}\subseteq\mathcal{V}\times\mathcal{V}$ is the set of undirected communication links, and $\mathcal{A}=[a_{ij}]$ is the associated weighted adjacency matrix. An undirected edge $(j,i)\in\mathcal{E}$ indicates that UAVs i and j can exchange information with each other. Accordingly, the neighbor set of UAV i is defined as $\mathcal{N}_i=\{j\in\mathcal{V}\mid(j,i)\in\mathcal{E}\}$. The overall leader–follower interaction topology is represented by a directed graph $\bar{G}$ with a node set $\bar{\mathcal{V}}=\{0\}\cup\mathcal{V}$, where node 0 represents the virtual leader and each node $i \in \mathcal{V}$ corresponds to a follower UAV. The graph $\bar{\mathcal{G}}$ is assumed to include at least one directed spanning tree.

The inner–outer-loop structure is employed to facilitate controller design for the multi-quadrotor UAVs. The outer (position) loop generates the desired thrust and attitude commands for the inner loop. The inner (attitude) loop, typically implemented by an onboard proportional–integral–derivative (PID) module, ensures fast attitude stabilization and tracking. This cascaded architecture enables outer-loop trajectory tracking for formation and obstacle avoidance tasks while preserving the fast response and robustness of the inner-loop attitude dynamics. The position loop model of the ith multi-quadrotor UAV is given by

$$\ddot{\boldsymbol{q}}_i = \boldsymbol{R}_i \frac{\boldsymbol{F}_{bi}}{m_i} - \boldsymbol{G} + \boldsymbol{d}_i^p,\ i \in \mathcal{V}. \tag{1}$$

where $\ddot{\boldsymbol{q}}_i = [\ddot{x}_i, \ddot{y}_i, \ddot{z}_i]^{\mathrm{T}}$ denotes the translational acceleration expressed in $\mathcal{F}_{\rceil}$ and $\boldsymbol{q}_i = [x_i, y_i, z_i]^{\mathrm{T}}$ represents the position vector of the i-th UAV in $\mathcal{F}_{\rceil}$. The thrust vector in $\mathcal{F}_{\lfloor}$ is $\boldsymbol{F}_{bi} = [0,0,F_i]^{\mathrm{T}}$, where F_i is the total thrust acting along the O_bZ_b-axis. Here, m_i represents the mass of UAV i, $\boldsymbol{G} = [0,0,g]^{\mathrm{T}}$ denotes the gravity vector, and $\boldsymbol{d}_i^p \in \mathbb{R}^3$ denotes the lumped disturbance accounting for external disturbances and model uncertainties. Moreover, $\boldsymbol{R}_i$ denotes the rotation matrix from $\mathcal{F}_{\lfloor}$ to $\mathcal{F}_{\rceil}$, which is expressed as

$$\boldsymbol{R}_i = \begin{bmatrix} c\theta_i c\psi_i & c\psi_i s\theta_i s\phi_i - s\psi_i c\phi_i & c\psi_i s\theta_i c\phi_i + s\psi_i s\phi_i \\ c\theta_i s\psi_i & s\psi_i s\theta_i s\phi_i + c\psi_i c\phi_i & s\psi_i s\theta_i c\phi_i - c\psi_i s\phi_i \\ -s\theta_i & s\phi_i c\theta_i & c\phi_i c\theta_i \end{bmatrix},\ i \in \mathcal{V}. \tag{2}$$

where $c \triangleq \cos$, $s \triangleq \sin$, and ϕ_i, θ_i, and ψ_i are the Euler angles of UAV i.

To address the underactuation of the position subsystem, the virtual control input $\boldsymbol{u}_i = \boldsymbol{R}_i \frac{\boldsymbol{F}_{bi}}{m_i}$ is defined, where $\boldsymbol{u}_i = [u_{xi}, u_{yi}, u_{zi}]^{\mathrm{T}}$, $i \in \mathcal{V}$. Then, the translational dynamics of the ith UAV are given by

$$\begin{aligned} \dot{\boldsymbol{q}}_i &= \boldsymbol{v}_i, \\ \dot{\boldsymbol{v}}_i &= \boldsymbol{u}_i - \boldsymbol{G} + \boldsymbol{d}_i^p,\ i \in \mathcal{V}. \end{aligned} \tag{3}$$

The Euler-angle kinematics satisfy $\dot{\boldsymbol{\Theta}}_i = \boldsymbol{T}(\boldsymbol{\Theta}_i)\omega_i$, where $\boldsymbol{\Theta}_i = [\phi_i, \theta_i, \psi_i]^{\mathrm{T}}$ collects the roll, pitch, and yaw angles, $\dot{\boldsymbol{\Theta}}_i = [\dot{\phi}_i, \dot{\theta}_i, \dot{\psi}_i]^{\mathrm{T}}$ denotes the Euler-angle rate vector, $\boldsymbol{\omega}_i = [\omega_{x_i}, \omega_{y_i}, \omega_{z_i}]^{\mathrm{T}}$ denotes the angular velocity expressed in $\mathcal{F}_{\lfloor}$, and $\boldsymbol{T}(\boldsymbol{\Theta}_i)$ is the associated transformation matrix given by

$$\boldsymbol{T}(\boldsymbol{\Theta}_i) = \begin{bmatrix} 1 & t\theta_i s\phi_i & t\theta_i c\phi_i \\ 0 & c\phi_i & -s\phi_i \\ 0 & \dfrac{s\phi_i}{c\theta_i} & \dfrac{c\phi_i}{c\theta_i} \end{bmatrix},\ i \in \mathcal{V}. \tag{4}$$

where $c \triangleq \cos$, $s \triangleq \sin$, and $t \triangleq \tan$.

The attitude dynamics of the ith multi-quadrotor UAV under lumped disturbances are described by the following equation:

$$J_i\dot{\omega}_i + \omega_i \times (J_i\omega_i) = \boldsymbol{\tau}_i + \boldsymbol{d}_i^a,\ i \in \mathcal{V}. \tag{5}$$

where $J_i = \mathrm{diag}\{J_{xx_i}, J_{yy_i}, J_{zz_i}\}$ is the inertia matrix, $\boldsymbol{\tau}_i = [\tau_{x_i}, \tau_{y_i}, \tau_{z_i}]^{\mathrm{T}}$ denotes the control moment vector in $\mathcal{F}_{\lfloor}$, and $\boldsymbol{d}_i^a = [d_i^\phi, d_i^\theta, d_i^\psi]^{\mathrm{T}}$ represents the lumped disturbance vector of the attitude loop.

Remark 1. *The obstacle is modeled in the inertial-reference frame $\mathcal{F}_{\rceil}$ as a vertical cylinder capped by an upper hemisphere. The center of the cylinder base is denoted by $\boldsymbol{c} = [x_c, y_c, z_c]^{\mathrm{T}} \in \mathbb{R}^3$, where $z_c = 0$ when the obstacle rests on the ground plane. The cylinder radius and height are $r_o > 0$ and $h_o > 0$, respectively. The cylinder–hemisphere model provides a compact and practical geometric representation for common 3D obstacles. The hemispherical top removes the sharp rim of a pure cylinder, yielding a smoother boundary and well-defined repulsive directions near the top region. Moreover, the repulsive-force computation for both the cylindrical and hemispherical parts can be carried out using a unified formula, which reduces computational complexity and facilitates real-time AAPF-based trajectory planning.*

Problem formulation

A team of N multi-quadrotor UAVs, indexed by $\mathcal{V} = \{1,\ldots,N\}$, is considered to operate in a cluttered 3D environment containing cylinder–hemisphere obstacles. The formation center is selected as a virtual leader, whose motion is described by the first-order kinematics

$$\dot{\boldsymbol{q}}_0 = \boldsymbol{v}_0 \tag{6}$$

where $\boldsymbol{q}_0 = [x_0, y_0, z_0]^{\mathrm{T}} \in \mathbb{R}^3$ and $\boldsymbol{v}_0 = [v_{x0}, v_{y0}, v_{z0}]^{\mathrm{T}} \in \mathbb{R}^3$ denote the virtual leader position and velocity, respectively, with $\boldsymbol{v}_0$ generated by the AAPF-based planner to achieve 3D obstacle avoidance.

Conventional schemes enforce formation coordination directly on the states of the multi-quadrotor UAVs, thereby coupling coordination with tracking transients and uncertainties. A distributed reference signal generator is developed over a network of second-order virtual agents to decouple reference generation from tracking. The virtual agent network inherits the communication topology of the multi-quadrotor UAV system. Through local information exchanges, it propagates the leader reference and generates reference signals for all multi-quadrotor UAVs. The dynamics of the virtual agent are formulated as

$$\begin{aligned} \dot{\boldsymbol{q}}_i^* &= \boldsymbol{v}_i^*, \\ \dot{\boldsymbol{v}}_i^* &= \boldsymbol{u}_i^*,\ i \in \mathcal{V}. \end{aligned} \tag{7}$$

where $\boldsymbol{u}_i^* = [u_{xi}^*, u_{yi}^*, u_{zi}^*]^{\mathrm{T}} \in \mathbb{R}^3$ is the control input, $\boldsymbol{q}_i^* = [x_i^*, y_i^*, z_i^*]^{\mathrm{T}}$ and $\boldsymbol{v}_i^* = [v_{xi}^*, v_{yi}^*, v_{zi}^*]^{\mathrm{T}}$ represent the position and velocity of the i-th virtual agent, respectively.

The objective is to guide the multi-quadrotor UAV formation from a given initial position to a desired goal in a 3D obstacle environment while maintaining the prescribed formation configuration and ensuring obstacle avoidance. A hierarchical distributed formation obstacle avoidance control scheme is proposed, as depicted in Fig. 1. At the *reference signal generation layer*, an AAPF-based planner generates a 3D obstacle avoidance trajectory for the virtual leader $\boldsymbol{q}_0$ such that the formation enclosing sphere remains collision-free, i.e., the clearance distance between the surfaces of the formation enclosing sphere and the obstacle satisfies $d_{\mathrm{obs}}(\boldsymbol{q}_0) = \|\boldsymbol{q}_0 - \boldsymbol{q}_{\mathrm{obs}}(\boldsymbol{q}_0)\|_2 - r_o - r_f > 0$. Here, the formation is enclosed by $\mathcal{B}(\boldsymbol{q}_0, r_f)$ centered at $\boldsymbol{q}_0$, where the formation radius satisfies $\|\boldsymbol{q}_i - \boldsymbol{q}_0\|_2 \le r_f$, equivalently $r_f = \max_{i \in \mathcal{V}} \|\boldsymbol{q}_i - \boldsymbol{q}_0\|_2$. Meanwhile, a distributed reference signal generator propagates $(\boldsymbol{q}_0, \boldsymbol{v}_0)$ to a network of second-order virtual agents through local communication and incorporates the prescribed offsets $\boldsymbol{h}_i = [h_{xi}, h_{yi}, h_{zi}]^{\mathrm{T}}$, i.e., the desired relative displacement of UAV i with respect to the virtual leader, thereby yielding formation-consistent references that satisfy $\lim_{t\to+\infty} \|\boldsymbol{q}_i^*(t) - \boldsymbol{q}_0(t) - \boldsymbol{h}_i\|_2 = 0$ and $\lim_{t\to+\infty} \|\boldsymbol{v}_i^*(t) - \boldsymbol{v}_0(t)\|_2 = 0$. At the *multi-quadrotor UAV trajectory tracking layer*, each UAV employs a local composite controller to track its reference trajectory, thereby ensuring formation maintenance and safe obstacle avoidance in the 3D obstacle environment.

Main results

AAPF design

The AAPF method is utilized for 3D motion planning. The goal generates an attractive potential, whereas obstacles generate repulsive potentials. Formation-level safety is enforced by enclosing

https://doi.org/10.48130/mav-0026-0004

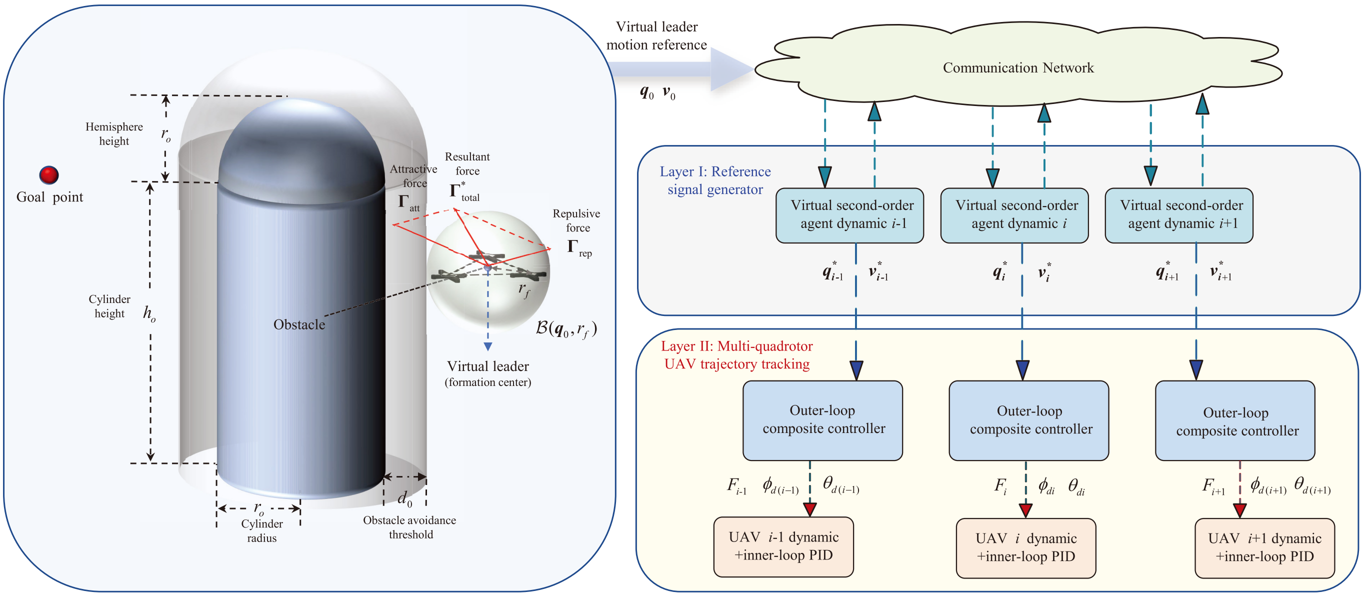

Fig. 1 Block diagram of the hierarchical distributed formation obstacle avoidance control scheme.

the formation within a safety sphere and activating the repulsive action when the sphere-obstacle clearance falls below a prescribed obstacle avoidance threshold. The virtual leader advances in the direction of the resultant force, guiding the formation toward the target while avoiding obstacles.

Attractive field and force design

The attractive potential is expressed as[25]

$$U_{\mathrm{att}}(\boldsymbol{q}_0) = \frac{1}{2} K_{\mathrm{att}}\, d^2_{\mathrm{goal}}(\boldsymbol{q}_0, \boldsymbol{q}_{\mathrm{goal}}) \tag{8}$$

where $\boldsymbol{q}_0$ represents the virtual leader's position and $\boldsymbol{q}_{\mathrm{goal}} = [x_g, y_g, z_g]^{\mathrm{T}}$ denotes its desired goal position. The Euclidean distance from the virtual leader to the goal is defined as $d_{\mathrm{goal}}(\boldsymbol{q}_0, \boldsymbol{q}_{\mathrm{goal}}) = \|\boldsymbol{q}_0 - \boldsymbol{q}_{\mathrm{goal}}\|_2$, and $K_{\mathrm{att}} > 0$ is the attractive gain.

The attractive force is given by

$$\begin{aligned} \boldsymbol{\Gamma}_{\mathrm{att}}(\boldsymbol{q}_0) &= -\nabla U_{\mathrm{att}}(\boldsymbol{q}_0) \\ &= -K_{\mathrm{att}}(\boldsymbol{q}_0 - \boldsymbol{q}_{\mathrm{goal}}). \end{aligned} \tag{9}$$

Repulsive field and force design

The equivalent obstacle center $\boldsymbol{q}_{\mathrm{obs}}(\boldsymbol{q}_0)$ is introduced to unify the repulsive action for the cylinder and hemisphere, and it is determined by the virtual leader position $\boldsymbol{q}_0$:

$$\boldsymbol{q}_{\mathrm{obs}}(\boldsymbol{q}_0) = \begin{cases} [x_c, y_c, z_0]^{\mathrm{T}}, & z_0 \le z_c + h_o\ , \\ \boldsymbol{c} + [0, 0, h_o]^{\mathrm{T}}, & z_0 > z_c + h_o\ , \end{cases} \tag{10}$$

where z_0 is the virtual leader's altitude, h_o is the cylinder height, and $\boldsymbol{c} = [x_c, y_c, z_c]^{\mathrm{T}} \in \mathbb{R}^3$ represents the center of the cylinder base.

The repulsive term is activated when the formation-enclosing sphere enters the obstacle-avoidance region. Therefore, the repulsive potential is defined as

$$U_{\mathrm{rep}}(\boldsymbol{q}_0) = \begin{cases} \dfrac{1}{2}\left(\dfrac{1}{d_{\mathrm{obs}}(\boldsymbol{q}_0)} - \dfrac{1}{d_0}\right)^2, & d_{\mathrm{obs}}(\boldsymbol{q}_0) \le d_0\ , \\ 0, & d_{\mathrm{obs}}(\boldsymbol{q}_0) > d_0\ , \end{cases} \tag{11}$$

where $d_0 > 0$ denotes the obstacle avoidance threshold, i.e., the distance between the obstacle surface and the boundary of the avoidance region. The condition $d_{\mathrm{obs}}(\boldsymbol{q}_0) \le d_0$ indicates that the formation-enclosing sphere has entered the avoidance region, and thus the repulsive potential is activated to generate an avoidance action.

Remark 2. *The 3D obstacle avoidance is implemented at the formation level by enclosing the multi-quadrotor UAV formation within $\mathcal{B}(\boldsymbol{q}_0, r_f)$. For a cylinder-hemisphere obstacle standing on the ground plane, where $z_c = 0$, the equivalent obstacle center in* Eq. (10) *is chosen as $[x_c, y_c, z_0]^{\mathrm{T}}$ for $z_0 \le h_o$ and as $[x_c, y_c, h_o]^{\mathrm{T}}$ for $z_0 > h_o$, so that the repulsive action is consistently applied to both the cylindrical part and the hemispherical cap.*

The repulsive gain is adaptively adjusted as a distance-dependent function:

$$K^*_{\mathrm{rep}} = \begin{cases} K^{\min}_{\mathrm{rep}} + \Delta K_{\mathrm{rep}}\left(1 - \dfrac{d_{\mathrm{obs}}(\boldsymbol{q}_0)}{d_0}\right), & d_{\mathrm{obs}}(\boldsymbol{q}_0) \le d_0, \\ 0, & d_{\mathrm{obs}}(\boldsymbol{q}_0) > d_0. \end{cases} \tag{12}$$

where $\Delta K_{\mathrm{rep}} = K^{\max}_{\mathrm{rep}} - K^{\min}_{\mathrm{rep}}$, with $K^{\min}_{\mathrm{rep}}$ and $K^{\max}_{\mathrm{rep}}$ are the minimum and maximum repulsive gains, respectively.

The repulsive force is given by

$$\begin{aligned} \boldsymbol{\Gamma}_{\mathrm{rep}}(\boldsymbol{q}_0) &= -K^*_{\mathrm{rep}} \nabla U_{\mathrm{rep}}(\boldsymbol{q}_0) \\ &= \begin{cases} K^*_{\mathrm{rep}} \dfrac{1}{d^2_{\mathrm{obs}}(\boldsymbol{q}_0)}\left(\dfrac{1}{d_{\mathrm{obs}}(\boldsymbol{q}_0)} - \dfrac{1}{d_0}\right)\dfrac{\partial d_{\mathrm{obs}}(\boldsymbol{q}_0)}{\partial \boldsymbol{q}_0}, & d_{\mathrm{obs}}(\boldsymbol{q}_0) \le d_0, \\ 0, & d_{\mathrm{obs}}(\boldsymbol{q}_0) > d_0. \end{cases} \end{aligned} \tag{13}$$

Remark 3. *The repulsive gain is adjusted linearly between $K^{\min}_{\mathrm{rep}}$ and $K^{\max}_{\mathrm{rep}}$ according to the proximity to the obstacle. Specifically, as $d_{\mathrm{obs}}(\boldsymbol{q}_0)$ decreases from d_0 to 0, K^*_{rep} increases linearly from $K^{\min}_{\mathrm{rep}}$ to $K^{\max}_{\mathrm{rep}}$, yielding stronger repulsion near obstacles while preserving smooth transitions in the control action.*

Accordingly, the resultant force is computed as

$$\boldsymbol{\Gamma}^*_{\mathrm{total}}(\boldsymbol{q}_0) = \boldsymbol{\Gamma}_{\mathrm{att}}(\boldsymbol{q}_0) + \boldsymbol{\Gamma}_{\mathrm{rep}}(\boldsymbol{q}_0) \tag{14}$$

Remark 4. *In the traditional APF method, a fixed repulsive gain is typically selected. When the repulsive gain is chosen inappropriately, it may cause overly aggressive avoidance maneuvers near the safety boundary or result in an insufficient avoidance response, thereby increasing the risk of collision. Therefore, an adaptive repulsive gain mechanism is introduced, which reduces sensitivity to parameter tuning and mitigates chattering in the repulsive force.*

Distributed reference signal generator design

The virtual leader's control input is obtained from the resultant force generated by the AAPF method:

$$\begin{aligned}\dot{\boldsymbol{q}}_0 &= \boldsymbol{v}_0 \\ &= \boldsymbol{\Gamma}^*_{\text{total}}(\boldsymbol{q}_0)\end{aligned} \tag{15}$$

where $\boldsymbol{q}_0 = [x_0, y_0, z_0]^T \in \mathbb{R}^3$ and $\boldsymbol{v}_0 = [v_{x0}, v_{y0}, v_{z0}]^T \in \mathbb{R}^3$ represent the virtual leader's position and velocity, respectively.

Remark 5. *The obstacle avoidance trajectory is generated by planning the motion of the virtual leader* $\boldsymbol{q}_0$. *In the AAPF method, the virtual leader is treated as a kinematic agent driven by the resultant force* $\boldsymbol{\Gamma}^*_{\text{total}}(\boldsymbol{q}_0)$ *in* Eq. (15), *which is composed of an attractive term pulling the virtual leader toward the goal and a repulsive term preventing collisions with obstacles. For the cylinder–hemisphere obstacles, the repulsive direction is determined by the equivalent obstacle center in* Eq. (10). *The repulsive term is activated only when the surface-to-surface clearance* $d_{\text{obs}}(\boldsymbol{q}_0)$ *between the formation-enclosing sphere and the obstacle is less than or equal to the obstacle avoidance threshold distance* d_0. *Therefore,* Eq. (15) *provides a 3D obstacle avoidance reference trajectory for the virtual leader, which is subsequently embedded into the distributed reference signal generator to generate multi-quadrotor UAV reference trajectories.*

Assumption 1. *The virtual leader reference trajectory generated by the AAPF method is admissible (i.e., feasible for implementation). For analytical tractability, the virtual leader velocity is idealized as a constant vector in the subsequent stability analysis, i.e.,* $\dot{\boldsymbol{v}}_0(t) = \boldsymbol{0}_3$.

The distributed reference signal generator produces the formation obstacle avoidance reference trajectories for the multi-quadrotor UAVs as

$$\dot{\boldsymbol{q}}_i^* = \boldsymbol{v}_i^* - \mu_1\left\{\sum_{j\in N_i} a_{ij}\left[(\boldsymbol{q}_i^* - \boldsymbol{h}_i) - (\boldsymbol{q}_j^* - \boldsymbol{h}_j)\right] + b_i\left[\boldsymbol{q}_i^* - (\boldsymbol{q}_0 + \boldsymbol{h}_i)\right]\right\}, \tag{16}$$

$$\dot{\boldsymbol{v}}_i^* = -\mu_2\left[\sum_{j\in N_i} a_{ij}\left(\boldsymbol{v}_i^* - \boldsymbol{v}_j^*\right) + b_i(\boldsymbol{v}_i^* - \boldsymbol{v}_0)\right],\ i\in\mathcal{V}. \tag{17}$$

where $\boldsymbol{q}_i^* = [x_i^*, y_i^*, z_i^*]^T \in \mathbb{R}^3$ and $\boldsymbol{v}_i^* = [v_{xi}^*, v_{yi}^*, v_{zi}^*]^T \in \mathbb{R}^3$ represent the position and velocity generated by the generator, respectively, and $\mu_1, \mu_2 > 0$ are design gains. Moreover, $\boldsymbol{h}_i \in \mathbb{R}^3$ and $\boldsymbol{h}_j \in \mathbb{R}^3$ are the formation configuration vectors of the i-th and j-th virtual agents with respect to the virtual leader, respectively.

The formation tracking errors of the generator are defined as

$$\begin{aligned}\tilde{\boldsymbol{q}}_i &= \boldsymbol{q}_i^* - (\boldsymbol{q}_0 + \boldsymbol{h}_i), \\ \tilde{\boldsymbol{v}}_i &= \boldsymbol{v}_i^* - \boldsymbol{v}_0,\ i\in\mathcal{V}.\end{aligned} \tag{18}$$

Based on Eqs. (16)–(18), the formation tracking error system is

$$\begin{aligned}\dot{\tilde{\boldsymbol{q}}}_i &= \tilde{\boldsymbol{v}}_i - \mu_1\left[\sum_{j\in N_i} a_{ij}\left(\tilde{\boldsymbol{q}}_i - \tilde{\boldsymbol{q}}_j\right) + b_i\tilde{\boldsymbol{q}}_i\right], \\ \dot{\tilde{\boldsymbol{v}}}_i &= -\mu_2\left[\sum_{j\in N_i} a_{ij}\left(\tilde{\boldsymbol{v}}_i - \tilde{\boldsymbol{v}}_j\right) + b_i\tilde{\boldsymbol{v}}_i\right],\ i\in\mathcal{V}.\end{aligned} \tag{19}$$

As the x, y, and z components of the generator formation tracking error are decoupled, the one-dimensional analysis can be directly extended to the 3D case. The one-dimensional error dynamics are given by

$$\begin{aligned}\dot{\tilde{\boldsymbol{q}}} &= \tilde{\boldsymbol{v}} - \mu_1 M\tilde{\boldsymbol{q}}, \\ \dot{\tilde{\boldsymbol{v}}} &= -\mu_2 M\tilde{\boldsymbol{v}}.\end{aligned} \tag{20}$$

where $\tilde{\boldsymbol{q}} = [\tilde{q}_1, \ldots, \tilde{q}_N]^T \in \mathbb{R}^N$ and $\tilde{\boldsymbol{v}} = [\tilde{v}_1, \ldots, \tilde{v}_N]^T \in \mathbb{R}^N$.

Proposition 1. *If Assumption 1 is satisfied, the origin of the error dynamics associated with the distributed reference signal generator given by* Eqs (16) and (17) *is exponentially stable. The formation position and velocity tracking errors satisfy* $\lim_{t\to+\infty}\tilde{\boldsymbol{q}}(t) = \boldsymbol{0}_N$ *and* $\lim_{t\to+\infty}\tilde{\boldsymbol{v}}(t) = \boldsymbol{0}_N$. *Equivalently, for each virtual agent* $i\in\mathcal{V}$, *one has* $\lim_{t\to+\infty}\left\|\boldsymbol{q}_i^*(t) - \boldsymbol{q}_0(t) - \boldsymbol{h}_i\right\|_2 = 0$ *and* $\lim_{t\to+\infty}\left\|\boldsymbol{v}_i^*(t) - \boldsymbol{v}_0(t)\right\|_2 = 0$. *Consequently, the generator achieves the desired formation obstacle avoidance configuration as* $t \to +\infty$.

Proof. The formation tracking error dynamics in Eq. (20) can be expressed in the following compact form:

$$\begin{bmatrix}\dot{\tilde{\boldsymbol{q}}} \\ \dot{\tilde{\boldsymbol{v}}}\end{bmatrix} = \begin{bmatrix}-\mu_1 M & I_N \\ \boldsymbol{0}_{N\times N} & -\mu_2 M\end{bmatrix}\begin{bmatrix}\tilde{\boldsymbol{q}} \\ \tilde{\boldsymbol{v}}\end{bmatrix} = D\begin{bmatrix}\tilde{\boldsymbol{q}} \\ \tilde{\boldsymbol{v}}\end{bmatrix} \tag{21}$$

The augmented error state is defined as $\boldsymbol{\delta} = \begin{bmatrix}\tilde{\boldsymbol{q}}^{\mathrm{T}}, \tilde{\boldsymbol{v}}^{\mathrm{T}}\end{bmatrix}^{\mathrm{T}} \in \mathbb{R}^{2N}$ so that Eq. (21) can be rewritten as $\dot{\boldsymbol{\delta}} = D\boldsymbol{\delta}$, where $D \in \mathbb{R}^{2N\times 2N}$. Based on Lemma 1 and the conditions $\mu_1 > 0$ and $\mu_2 > 0$, the matrix D is Hurwitz. Therefore, for any given symmetric positive definite matrix $Q_f \in \mathbb{R}^{2N\times 2N}$, there exists a unique symmetric positive definite matrix $P_f \in \mathbb{R}^{2N\times 2N}$ such that

$$D^T P_f + P_f D = -Q_f \tag{22}$$

The Lyapunov function is given by

$$V_f = \boldsymbol{\delta}^T P_f \boldsymbol{\delta} \tag{23}$$

Taking the time derivative of Eq. (23) yields

$$\begin{aligned}\dot{V}_f &= \dot{\boldsymbol{\delta}}^T P_f \boldsymbol{\delta} + \boldsymbol{\delta}^T P_f \dot{\boldsymbol{\delta}} \\ &= -\boldsymbol{\delta}^T Q_f \boldsymbol{\delta} \\ &\le -\lambda_{\min}(Q_f)\|\boldsymbol{\delta}\|_2^2\end{aligned} \tag{24}$$

From Eq. (24) and $\lambda_{\min}(P_f)\|\boldsymbol{\delta}\|_2^2 \le V_f \le \lambda_{\max}(P_f)\|\boldsymbol{\delta}\|_2^2$, it holds that

$$\begin{aligned}\dot{V}_f &\le -\frac{\lambda_{\min}(Q_f)}{\lambda_{\max}(P_f)}V_f \\ &= -\kappa V_f\end{aligned} \tag{25}$$

where $\kappa = \dfrac{\lambda_{\min}(Q_f)}{\lambda_{\max}(P_f)} > 0$. It follows that $V_f(t)$ decays exponentially, i.e., $V_f(t) \le V_f(0)e^{-\kappa t}$, $\forall t \ge 0$. Hence, the origin of the formation tracking error system (21) is exponentially stable. Consequently, the formation position tracking error $\tilde{\boldsymbol{q}}(t)$ converges exponentially to $\boldsymbol{0}_N$, that is, $\lim_{t\to+\infty}\tilde{\boldsymbol{q}}(t) = \boldsymbol{0}_N$. Accordingly, $\lim_{t\to+\infty}\left\|\boldsymbol{q}_i^*(t) - \boldsymbol{q}_0(t) - \boldsymbol{h}_i\right\|_2 = 0$, $i\in\mathcal{V}$. Moreover, the formation velocity tracking error $\tilde{\boldsymbol{v}}(t)$ converges exponentially to $\boldsymbol{0}_N$, namely, $\lim_{t\to+\infty}\tilde{\boldsymbol{v}}(t) = \boldsymbol{0}_N$. Accordingly, $\lim_{t\to+\infty}\left\|\boldsymbol{v}_i^*(t) - \boldsymbol{v}_0(t)\right\|_2 = 0$, $i\in\mathcal{V}$. This completes the proof.

Multi-quadrotor UAVs trajectory tracking control design

The position subsystem is extended by treating the lumped disturbance as an additional state variable:

$$\begin{aligned}\dot{\boldsymbol{q}}_i &= \boldsymbol{v}_i, \\ \dot{\boldsymbol{v}}_i &= \boldsymbol{u}_i - \boldsymbol{G} + \boldsymbol{d}_i^p, \\ \dot{\boldsymbol{d}}_i^p &= \boldsymbol{\xi}_i,\ i\in\mathcal{V}.\end{aligned} \tag{26}$$

where $\boldsymbol{\xi}_i \in \mathbb{R}^3$ denotes the time derivative of the lumped disturbance and is unknown but bounded, i.e., $\|\boldsymbol{\xi}_i(t)\|_2 \le H_i$ for all $t \ge 0$, where $H_i > 0$ is a constant.

An ESO is designed to estimate the states and the lumped disturbance of the position subsystem:

$$\begin{aligned}\dot{\hat{\boldsymbol{q}}}_i &= \hat{\boldsymbol{v}}_i + \beta_1(\boldsymbol{q}_i - \hat{\boldsymbol{q}}_i), \\ \dot{\hat{\boldsymbol{v}}}_i &= \boldsymbol{u}_i - \boldsymbol{G} + \hat{\boldsymbol{d}}_i^p + \beta_2(\boldsymbol{q}_i - \hat{\boldsymbol{q}}_i), \\ \dot{\hat{\boldsymbol{d}}}_i^p &= \beta_3(\boldsymbol{q}_i - \hat{\boldsymbol{q}}_i),\ i\in\mathcal{V}.\end{aligned} \tag{27}$$

where β_1, β_2, $\beta_3 > 0$ are observer design gains.

The composite controller with disturbance estimation of the position loop is designed as follows:

https://doi.org/10.48130/mav-0026-0004

$$\boldsymbol{u}_i = \boldsymbol{G} - \hat{\boldsymbol{d}}_i^p + \boldsymbol{K}_{pi}(\boldsymbol{q}_i^* - \boldsymbol{q}_i) + \boldsymbol{K}_{di}(\boldsymbol{v}_i^* - \boldsymbol{v}_i) + \dot{\boldsymbol{v}}_i^*,\ i \in \mathcal{V}. \tag{28}$$

where $\boldsymbol{u}_i = [u_{xi}, u_{yi}, u_{zi}]^T$ denotes the control input vector and $\boldsymbol{K}_{pi} = \mathrm{diag}\{k_{pi,1}, k_{pi,2}, k_{pi,3}\}$ and $\boldsymbol{K}_{di} = \mathrm{diag}\{k_{di,1}, k_{di,2}, k_{di,3}\}$ denote the design gain matrices, respectively.

The inner loop adopts the PID controller for tracking the attitude angle. Based on the virtual acceleration control inputs and the desired yaw angle ψ_{di} (specified by the user), the desired total thrust, roll angle, and pitch angle are computed, respectively, as $F_i = m_i\sqrt{u_{xi}^2 + u_{yi}^2 + u_{zi}^2}$, $\phi_{di} = \arcsin\left[\frac{m_i}{F_i}(u_{xi}\sin\psi_{di} - u_{yi}\cos\psi_{di})\right]$, and $\theta_{di} = \arctan\left(\frac{u_{xi}\cos\psi_{di} + u_{yi}\sin\psi_{di}}{u_{zi}}\right)$, $i \in \mathcal{V}$.

Theorem 1. *For the position loop dynamics of the multi-quadrotor UAVs described by Eq.* (3) *in the presence of lumped disturbances, under Assumption 1, by designing the tracking controller represented by Eq.* (28) *together with the ESO* (Eq. 27)*, the positions and velocities of the multi-quadrotor UAVs achieve bounded tracking of the reference signals generated by the distributed reference signal generator given in Eqs* (16) and (17). *Then, the formation obstacle avoidance control goal is achieved.*

Proof. The ESO estimation errors are defined as

$$\begin{aligned}\tilde{\boldsymbol{q}}_{oi} &= \boldsymbol{q}_i - \hat{\boldsymbol{q}}_i,\\ \tilde{\boldsymbol{v}}_{oi} &= \boldsymbol{v}_i - \hat{\boldsymbol{v}}_i,\\ \tilde{\boldsymbol{d}}_i^p &= \boldsymbol{d}_i^p - \hat{\boldsymbol{d}}_i^p,\ i \in \mathcal{V}.\end{aligned} \tag{29}$$

Computing the time derivative of the estimation errors in Eq. (29) and substituting Eqs (26) and (27) yields

$$\begin{aligned}\dot{\tilde{\boldsymbol{q}}}_{oi} &= \tilde{\boldsymbol{v}}_{oi} - \beta_1\tilde{\boldsymbol{q}}_{oi},\\ \dot{\tilde{\boldsymbol{v}}}_{oi} &= \tilde{\boldsymbol{d}}_i^p - \beta_2\tilde{\boldsymbol{q}}_{oi},\\ \dot{\tilde{\boldsymbol{d}}}_i^p &= \boldsymbol{\xi}_i - \beta_3\tilde{\boldsymbol{q}}_{oi},\ i \in \mathcal{V}.\end{aligned} \tag{30}$$

The augmented estimation error vector is denoted by $\boldsymbol{\varepsilon}_i = [\tilde{\boldsymbol{q}}_{oi}^T, \tilde{\boldsymbol{v}}_{oi}^T, (\tilde{\boldsymbol{d}}_i^p)^T]^T \in \mathbb{R}^9$. To facilitate the stability analysis, the error dynamics can be compactly written as $\dot{\boldsymbol{\varepsilon}}_i = A_e\boldsymbol{\varepsilon}_i + E\boldsymbol{\xi}_i$, $i \in \mathcal{V}$, where the system matrices are defined as

$$A_e = \begin{bmatrix} -\beta_1 I_3 & I_3 & \mathbf{0}_{3\times3} \\ -\beta_2 I_3 & \mathbf{0}_{3\times3} & I_3 \\ -\beta_3 I_3 & \mathbf{0}_{3\times3} & \mathbf{0}_{3\times3} \end{bmatrix} \in \mathbb{R}^{9\times9} \tag{31}$$

$$E = \begin{bmatrix} \mathbf{0}_{3\times3} \\ \mathbf{0}_{3\times3} \\ I_3 \end{bmatrix} \in \mathbb{R}^{9\times3} \tag{32}$$

With $\omega_o > 0$ and the observer design gains chosen as $\beta_1 = 3\omega_o$, $\beta_2 = 3\omega_o^2$, and $\beta_3 = \omega_o^3$, the matrix A_e is Hurwitz and has all its eigenvalues equal to $-\omega_o$. Therefore, for any given symmetric positive definite matrix $Q_e \in \mathbb{R}^{9\times9}$, there exists a unique symmetric positive definite matrix $P_e \in \mathbb{R}^{9\times9}$ that satisfies the Lyapunov equation:

$$A_e^T P_e + P_e A_e = -Q_e \tag{33}$$

The following Lyapunov function is selected:

$$V_{oi} = \boldsymbol{\varepsilon}_i^T P_e \boldsymbol{\varepsilon}_i,\ i \in \mathcal{V}. \tag{34}$$

Taking the time derivative of Eq. (34) and invoking Lemma 2 give

$$\begin{aligned}\dot{V}_{oi} &= -\boldsymbol{\varepsilon}_i^T Q_e \boldsymbol{\varepsilon}_i + 2\boldsymbol{\varepsilon}_i^T P_e E\boldsymbol{\xi}_i\\ &\le -\lambda_{\min}(Q_e)\|\boldsymbol{\varepsilon}_i\|_2^2 + 2\|P_e E\|_2 H_i\|\boldsymbol{\varepsilon}_i\|_2\\ &\le -\frac{\lambda_{\min}(Q_e)}{2}\|\boldsymbol{\varepsilon}_i\|_2^2 + \frac{2\|P_e E\|_2^2 H_i^2}{\lambda_{\min}(Q_e)},\ i \in \mathcal{V}.\end{aligned} \tag{35}$$

By utilizing the bound $V_{oi} \le \lambda_{\max}(P_e)\|\boldsymbol{\varepsilon}_i\|_2^2$, one has

$$\dot{V}_{oi} \le -\alpha V_{oi} + \vartheta_i,\ i \in \mathcal{V}. \tag{36}$$

where $\alpha = \frac{\lambda_{\min}(Q_e)}{2\lambda_{\max}(P_e)}$ and $\vartheta_i = \frac{2\|P_e E\|_2^2 H_i^2}{\lambda_{\min}(Q_e)}$.

The solution of Eq. (36) satisfies

$$V_{oi}(t) \le V_{oi}(0)e^{-\alpha t} + \frac{\vartheta_i}{\alpha}(1 - e^{-\alpha t}),\ i \in \mathcal{V}. \tag{37}$$

From Eq. (37), $V_{oi}(t)$ is uniformly ultimately bounded (UUB), and thus the ESO estimation error $\boldsymbol{\varepsilon}_i$ is UUB.

Combining Eq. (37) with $\lambda_{\min}(P_e)\|\boldsymbol{\varepsilon}_i\|_2^2 \le V_{oi}$ yields

$$\|\boldsymbol{\varepsilon}_i(t)\|_2 \le \sqrt{\frac{\vartheta_i}{\alpha\lambda_{\min}(P_e)} + \frac{1}{\lambda_{\min}(P_e)}\left[V_{oi}(0) - \frac{\vartheta_i}{\alpha}\right]e^{-\alpha t}},\ i \in \mathcal{V}. \tag{38}$$

Therefore, for any $\zeta_{oi} > \sqrt{\frac{\vartheta_i}{\alpha\lambda_{\min}(P_e)}}$, there exists a constant $T_{oi} > 0$ such that for all $t > T_{oi}$, $\|\boldsymbol{\varepsilon}_i\|_2 \le \zeta_{oi}$. That is, the estimation error $\boldsymbol{\varepsilon}_i$ converges to the compact set $\Omega_{oi} = \{\boldsymbol{\varepsilon}_i \in \mathbb{R}^9 \mid \|\boldsymbol{\varepsilon}_i\|_2 \le \zeta_{oi}\}$, where ζ_{oi} can be rendered arbitrarily small by appropriately adjusting the observer bandwidth ω_o and satisfying the stability condition. This indicates that the estimation errors $\tilde{\boldsymbol{q}}_{oi}$, $\tilde{\boldsymbol{v}}_{oi}$, and $\tilde{\boldsymbol{d}}_i^p$ converge to a prescribed neighborhood of the origin.

The closed-loop tracking errors under the composite controller given by Eq. (28) are defined as

$$\begin{aligned}\boldsymbol{e}_{qi} &= \boldsymbol{q}_i^* - \boldsymbol{q}_i,\\ \boldsymbol{e}_{vi} &= \boldsymbol{v}_i^* - \boldsymbol{v}_i,\ i \in \mathcal{V}.\end{aligned} \tag{39}$$

Substituting Eq. (28) into Eq. (26) yields

$$\begin{aligned}\dot{\boldsymbol{v}}_i &= \boldsymbol{u}_i - \boldsymbol{G} + \boldsymbol{d}_i^p\\ &= \boldsymbol{K}_{pi}\boldsymbol{e}_{qi} + \boldsymbol{K}_{di}\boldsymbol{e}_{vi} + \tilde{\boldsymbol{d}}_i^p + \dot{\boldsymbol{v}}_i^*,\ i \in \mathcal{V}.\end{aligned} \tag{40}$$

Noting that $\dot{\boldsymbol{e}}_{vi} = \dot{\boldsymbol{v}}_i^* - \dot{\boldsymbol{v}}_i$, one has

$$\begin{aligned}\dot{\boldsymbol{e}}_{vi} &= \dot{\boldsymbol{v}}_i^* - \left(\boldsymbol{K}_{pi}\boldsymbol{e}_{qi} + \boldsymbol{K}_{di}\boldsymbol{e}_{vi} + \tilde{\boldsymbol{d}}_i^p + \dot{\boldsymbol{v}}_i^*\right)\\ &= -\boldsymbol{K}_{pi}\boldsymbol{e}_{qi} - \boldsymbol{K}_{di}\boldsymbol{e}_{vi} - \tilde{\boldsymbol{d}}_i^p,\ i \in \mathcal{V}.\end{aligned} \tag{41}$$

The closed-loop tracking error dynamics are given by

$$\begin{bmatrix} \dot{\boldsymbol{e}}_{qi} \\ \dot{\boldsymbol{e}}_{vi} \end{bmatrix} = \begin{bmatrix} \mathbf{0}_{3\times3} & I_3 \\ -\boldsymbol{K}_{pi} & -\boldsymbol{K}_{di} \end{bmatrix}\begin{bmatrix} \boldsymbol{e}_{qi} \\ \boldsymbol{e}_{vi} \end{bmatrix} + \begin{bmatrix} \mathbf{0}_{3\times1} \\ -\tilde{\boldsymbol{d}}_i^p \end{bmatrix},\ i \in \mathcal{V}. \tag{42}$$

The reduced system without $\tilde{\boldsymbol{d}}_i^p$ is considered

$$\begin{bmatrix} \dot{\boldsymbol{e}}_{qi} \\ \dot{\boldsymbol{e}}_{vi} \end{bmatrix} = \begin{bmatrix} \mathbf{0}_{3\times3} & I_3 \\ -\boldsymbol{K}_{pi} & -\boldsymbol{K}_{di} \end{bmatrix}\begin{bmatrix} \boldsymbol{e}_{qi} \\ \boldsymbol{e}_{vi} \end{bmatrix},\ i \in \mathcal{V}. \tag{43}$$

The error dynamics (Eq. 43) is a linear system. If the gain matrices $\boldsymbol{K}_{pi} = \mathrm{diag}\{k_{pi,1}, k_{pi,2}, k_{pi,3}\}$ and $\boldsymbol{K}_{di} = \mathrm{diag}\{k_{di,1}, k_{di,2}, k_{di,3}\}$ with $k_{pi,j} > 0$ and $k_{di,j} > 0$ for $j = 1,2,3$, then the associated system matrix is Hurwitz, and the origin of Eq. (43) is globally exponentially stable. Furthermore, Eq. (38) implies that there exists a constant $\bar{d}_i > 0$ such that $\sup_{t\ge0}\|\tilde{\boldsymbol{d}}_i^p(t)\|_2 \le \bar{d}_i$. According to Lemma 3, the system (Eq. 42) is ISS. Hence, the tracking errors $\boldsymbol{e}_{qi}$ and $\boldsymbol{e}_{vi}$ are bounded. This completes the proof.

Remark 6. *In the absence of measurement noise, if the lumped disturbance $\boldsymbol{d}_i^p(t)$ satisfies $\lim_{t\to+\infty}\dot{\boldsymbol{d}}_i^p(t) = \mathbf{0}_3$, then the corresponding estimation error satisfies $\lim_{t\to+\infty}\tilde{\boldsymbol{d}}_i^p(t) = \mathbf{0}_3$. Hence, the closed-loop position and velocity tracking errors asymptotically converge to the origin, i.e., $\lim_{t\to+\infty}\boldsymbol{e}_{qi}(t) = \mathbf{0}_3$ and $\lim_{t\to+\infty}\boldsymbol{e}_{vi}(t) = \mathbf{0}_3$.*

Experiments

Two experiments are presented to validate the effectiveness of the proposed hierarchical distributed control scheme for cooperative formation and obstacle avoidance. Based on the position-loop model in Eq. (3), the outer-loop translational dynamics of the multi-quadrotor UAVs are modeled as second-order integrator dynamics.

The obstacle avoidance trajectory for the virtual leader is then generated using the AAPF method, as described in Eq. (15). Then, the distributed reference signal generator given in Eqs (16) and (17) produces the desired formation obstacle avoidance trajectories for all multi-quadrotor UAVs. The composite controller in Eq. (28) drives each multi-quadrotor UAV to track its desired trajectory. The corresponding attitude commands are then obtained by a small-angle-based inversion, which yields the required thrust and the desired roll and pitch angles, while the desired yaw angle is set to zero. These commands are applied to the inner-loop attitude dynamics, where the onboard PID module performs attitude tracking.

A. Experimental setup: In the experiments, a comprehensive platform is built around the Crazyflie 2.1 multi-quadrotor UAV[41] and a vision-based motion capture system. The markers attached to each multi-quadrotor UAV are utilized by the motion capture system to reliably identify individual UAVs and precisely reconstruct their real-time 3D positions. The overall data flow of the experimental platform and the communication topology of the three multi-quadrotor UAVs are depicted in Fig. 2. Crazyflie 2.1 uses an STM32F405 as the main MCU and communicates with the ground-station PC over a 2.4 GHz link through a Crazyradio dongle connected to the PC. A motion capture system consisting of eight MC1300 cameras from CHINGMU Company provides localization for the multi-quadrotor UAVs. The ground-station PC reconstructs the 3D position, encapsulates the position data into a predefined Robot Operating System (ROS) message, and publishes it to a dedicated ROS topic. The proposed hierarchical distributed formation obstacle avoidance control scheme then subscribes to this topic and executes the control algorithm.

The three multi-quadrotor UAVs are initially positioned at $\boldsymbol{q}_1(0) = [0, 0, 0.4]^T\,\mathrm{m}$, $\boldsymbol{q}_2(0) = [0, 0.2, 0.4]^T\,\mathrm{m}$, and $\boldsymbol{q}_3(0) = [0, -0.2, 0.4]^T\,\mathrm{m}$. The start and goal positions of the virtual leader are set to $[0, 0, 0.4]^T\,\mathrm{m}$ and $[2.4, 1.4, 0.6]^T\,\mathrm{m}$, respectively. Let the obstacles be indexed by $n \in \{1, 2\}$ and modeled as capped cylinders. In *experimental example 1*, the cylinder-base centers are located at $(x_{c,n}, y_{c,n}) \in \{(1.00, 0.45), (1.75, 1.70)\}\,\mathrm{m}$, with corresponding radii $r_{o,n} \in \{0.14, 0.225\}\,\mathrm{m}$. The heights of the cylinders are $h_{o,n} \in \{0.4, 1\}\,\mathrm{m}$. In *experimental example 2*, $(x_{c,n}, y_{c,n}) \in \{(1.00, 0.45), (1.55, 1.70)\}\,\mathrm{m}$, whereas the radii and heights of the cylinders remain $r_{o,n} \in \{0.14, 0.225\}\,\mathrm{m}$ and $h_{o,n} \in \{0.4, 1\}\,\mathrm{m}$, respectively. The formation offsets of the multi-quadrotor UAVs relative to the virtual leader are $\boldsymbol{h}_1 = [0.10, 0.00, 0.00]^T\,\mathrm{m}$, $\boldsymbol{h}_2 = [-0.12, 0.25, 0.00]^T\,\mathrm{m}$, and $\boldsymbol{h}_3 = [-0.12, -0.25, 0.00]^T\,\mathrm{m}$, respectively. The AAPF parameters are set to $K_{\mathrm{att}} = 0.1$, $K_{\mathrm{rep}}^{\min} = 0.05$, and $K_{\mathrm{rep}}^{\max} = 0.3$. The obstacle avoidance threshold distance is set to $d_0 = 0.12\,\mathrm{m}$ in *experimental example 1* and $d_0 = 0.15\,\mathrm{m}$ in *experimental example 2*. The distributed reference signal generator parameters are set to $\mu_1 = 0.1$ and $\mu_2 = 2$. The ESO gains are chosen as $\beta_1 = 15$, $\beta_2 = 75$, and $\beta_3 = 125$. The controller gains are $\boldsymbol{K}_{pi} = \mathrm{diag}\{4.5, 4.5, 5.4\}$ and $\boldsymbol{K}_{di} = \mathrm{diag}\{5, 5, 3\}$, $i \in \mathcal{V}$.

B. Experimental example 1: Results and analysis of cooperative formation obstacle avoidance in sparse obstacle environments.

The experimental results of example 1 are presented in Figs 3a, 4a, 5, and 6. As shown in Figs 3a and 4a, the proposed hierarchical distributed formation obstacle avoidance control scheme enables the three multi-quadrotor UAVs to maintain the desired triangular formation configuration while executing 3D obstacle avoidance maneuvers (overflight and detouring). The responses of the distributed reference signal generator in Eqs (16) and (17) are plotted in Fig. 5, where the second-order virtual followers maintain the desired relative positions with respect to the virtual leader and achieve velocity consensus. Figure 6 depicts the trajectory tracking errors under the composite controller given in Eq. (28). The results show that both the position and velocity tracking errors remain bounded and converge to small residual neighborhoods around the origin, confirming effective tracking of the formation obstacle

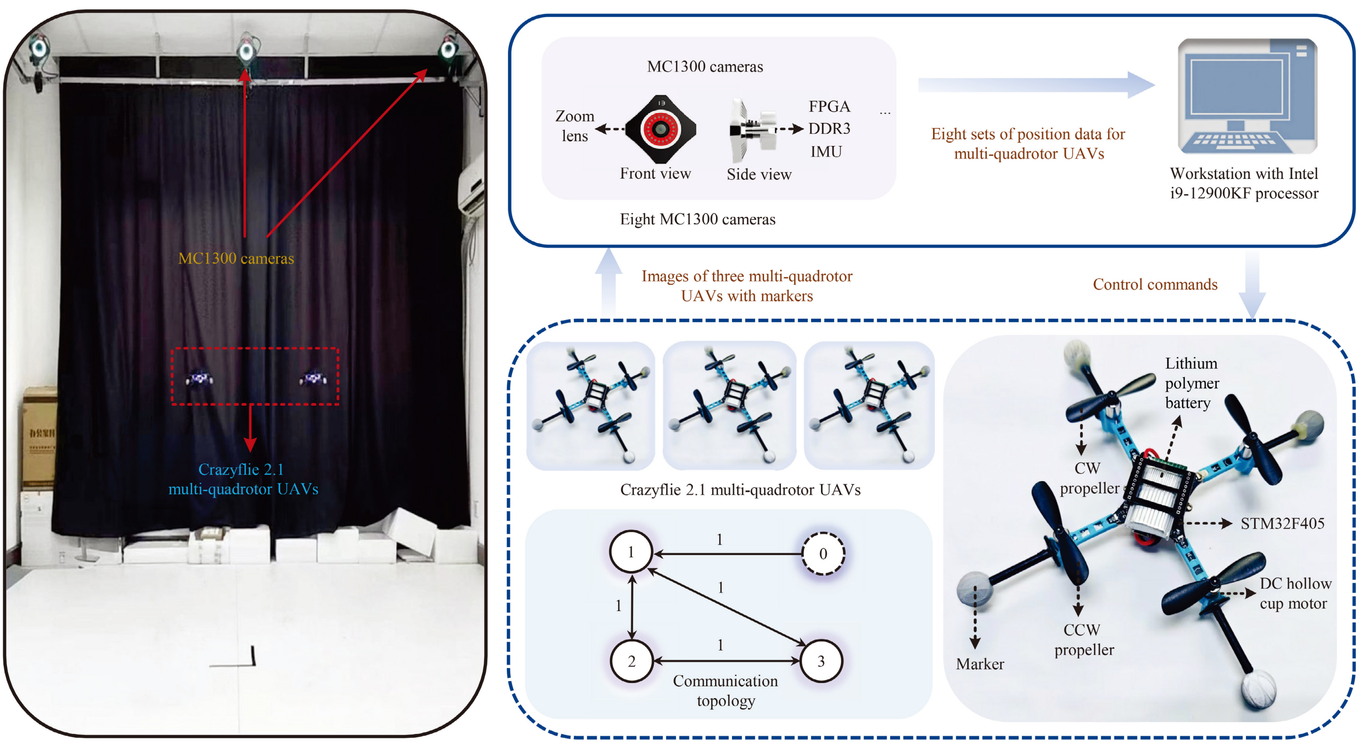

Fig. 2 The experimental platform.

https://doi.org/10.48130/mav-0026-0004

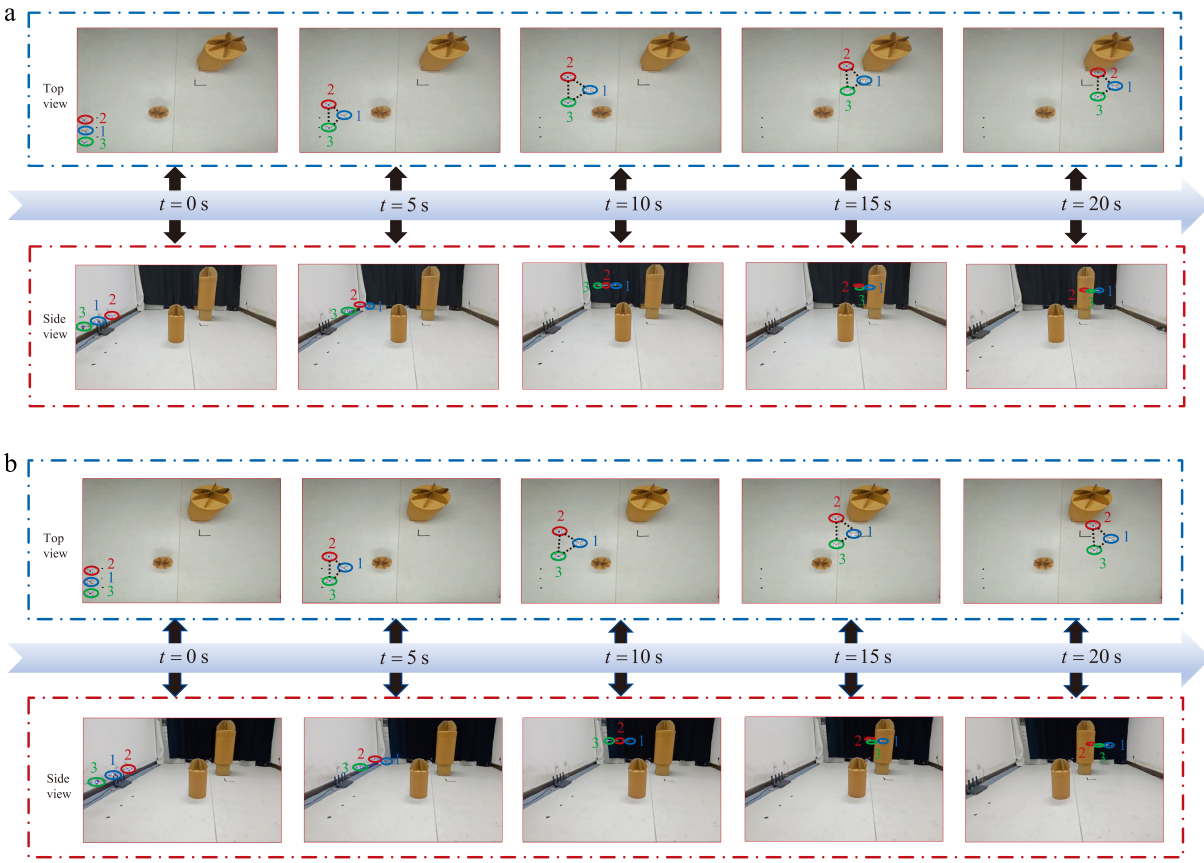

Fig. 3 Experimental images and multi-quadrotor UAV positions at different time instants. (a) Real-time positions of the multi-quadrotor UAVs in example 1. (b) Real-time positions of the multi-quadrotor UAVs in example 2.

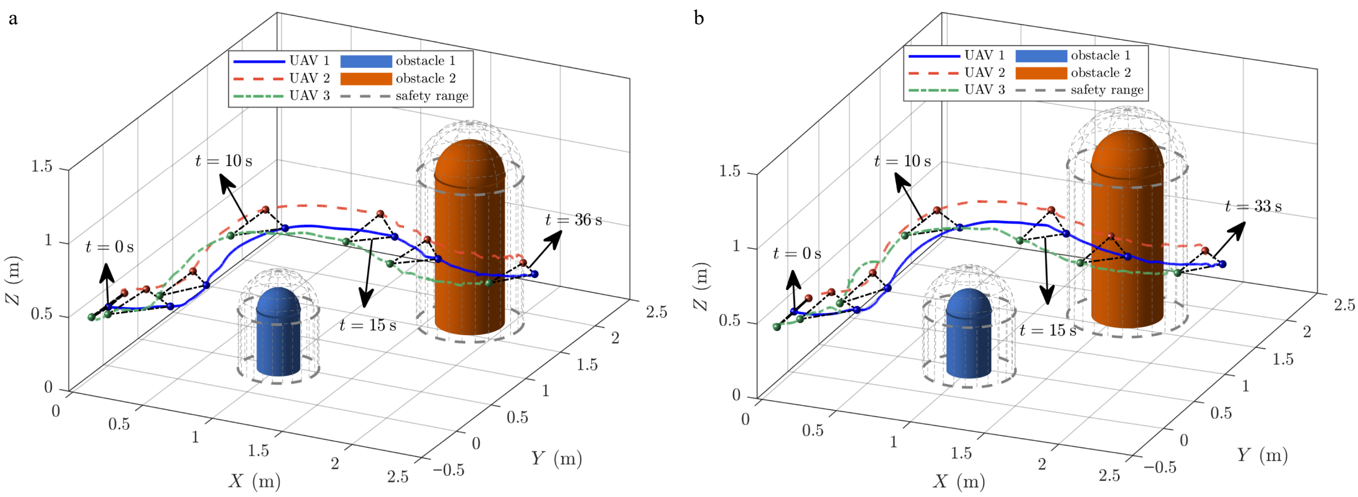

Fig. 4 Trajectories of the multi-quadrotor UAVs in 3D space. (a) 3D trajectories of the formation obstacle avoidance maneuver in example 1. (b) 3D trajectories of the formation obstacle avoidance maneuver in example 2.

avoidance references produced by Eqs (16) and (17). Overall, these results validate the effectiveness and feasibility of the proposed scheme in sparse obstacle environments.

C. Experimental example 2: Results and analysis of cooperative formation obstacle avoidance in dense obstacle environments.

The two obstacles in experimental example 2 are closer than those in experimental example 1. Therefore, a stronger spatial constraint is imposed on the multi-quadrotor UAVs' formation obstacle avoidance trajectory. The experimental results of example 2 are presented in Figs 3b, 4b, 7, and 8. In dense obstacle environments, the proposed hierarchical distributed formation obstacle avoidance control scheme enables the three multi-quadrotor UAVs to perform 3D obstacle avoidance maneuvers (overflight and detouring) while maintaining the desired triangular formation, as illustrated in Figs 3b and 4b. Consequently, the formation configuration is maintained throughout the maneuver, and smooth trajectories are achieved even when obstacles are closely spaced, demonstrating the effectiveness and robustness of the proposed scheme

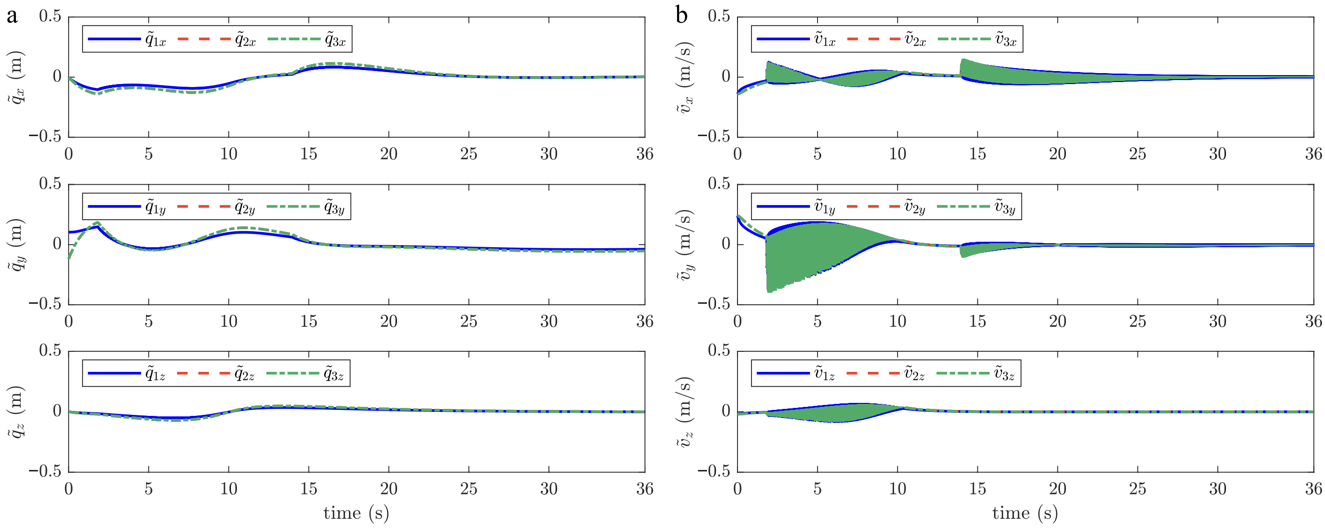

Fig. 5 Response curves of the formation tracking errors under the distributed reference signal generator given by Eqs. (16) and (17) in example 1. (a) Response curves of the formation position errors. (b) Response curves of the formation velocity errors.

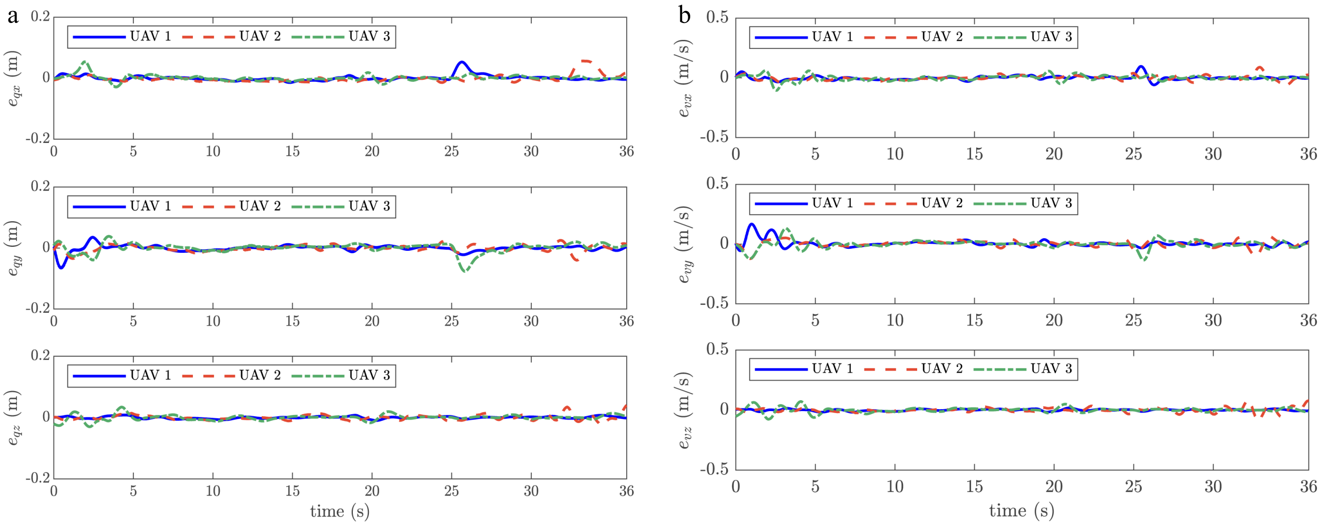

Fig. 6 Response curves of the multi-quadrotor UAVs' trajectory tracking errors under the composite controller given by Eq. (28) in example 1. (a) Response curves of the position tracking errors. (b) Response curves of the velocity tracking errors.

under strong 3D environmental constraints. The response curves of the distributed reference signal generator in Eqs (16) and (17) are presented in Fig. 7, indicating that the second-order virtual followers preserve the desired relative positions with respect to the virtual leader and achieve velocity consensus. The trajectory tracking error responses of the multi-quadrotor UAVs under the composite controller in Eq. (28) are presented in Fig. 8. It is observed that both the position and velocity tracking errors are bounded and converge to small neighborhoods around the origin. Hence, it is verified that the designed composite controller in Eq. (28) achieves robust trajectory tracking in dense obstacle environments. In summary, these experimental results demonstrate the effectiveness and feasibility of the proposed hierarchical distributed formation obstacle avoidance control scheme in both sparse and dense obstacle environments.

Conclusions

In this study, a hierarchical distributed control scheme is developed for multi-quadrotor UAVs that achieves cooperative formation while ensuring 3D obstacle avoidance. An adaptive repulsive gain mechanism is developed within the APF method, mitigating repulsive force jitter near boundaries and reducing the parameter sensitivity inherent in fixed gain designs. The proposed control scheme is composed of two layers, i.e., an upper-layer distributed reference signal generator for formation obstacle avoidance and a lower-layer composite controller for trajectory tracking of the multi-quadrotor UAVs. The two-layer structure improves design flexibility, and the stability analysis demonstrates exponential convergence of the upper-layer formation tracking errors and boundedness of the lower-layer trajectory tracking errors. Experimental results validate the proposed hierarchical distributed formation obstacle avoidance control scheme. Future work will be focused on hierarchical distributed formation obstacle avoidance control for multi-quadrotor systems subject to velocity constraints.

Author contributions

The authors confirm their contributions to the paper as follows: study conception and design: Liu Z, Wang X; data collection: Liu Z,

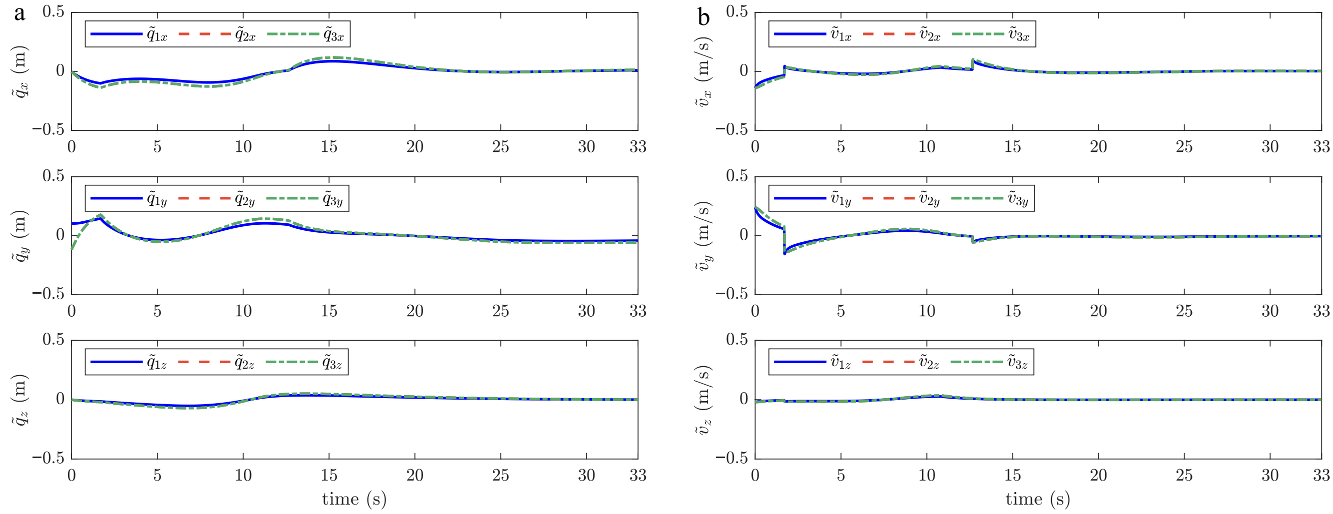

Fig. 7 Response curves of the formation tracking errors under the distributed reference signal generator given by Eqs (16) and (17) in example 2. (a) Response curves of the formation position errors. (b) Response curves of the formation velocity errors.

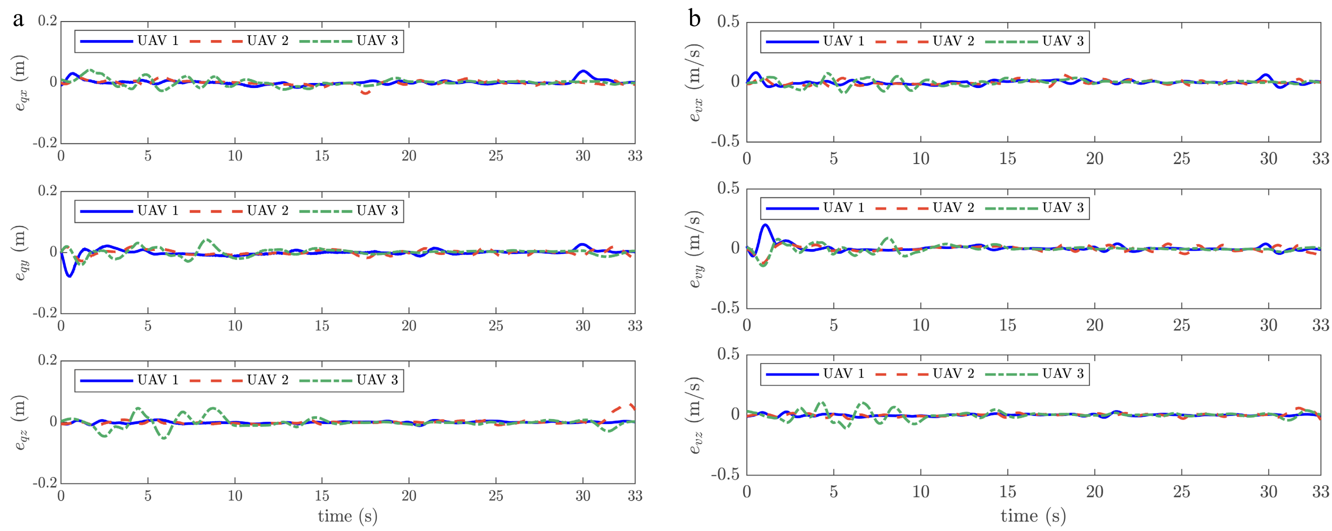

Fig. 8 Response curves of the multi-quadrotor UAVs' trajectory tracking errors under the composite controller given by Eq. (28) in example 2. (a) Response curves of the position tracking errors. (b) Response curves of the velocity tracking errors.

Xie F; analysis and interpretation of the results: Liu Z, Wang X, Xie F; draft manuscript preparation: Liu Z. All authors reviewed the results and approved the final version of the manuscript.

Data availability

The datasets generated during and/or analyzed during the current study are available from the corresponding author on reasonable request.

Acknowledgments

This work was supported by the National Natural Science Foundation of China under Grants 62533012 and 62373099.

Conflict of interest

The authors declare that they have no conflict of interest.

Dates

Received 5 February 2026; Revised 13 March 2026; Accepted 9 April 2026; Published online 22 July 2026

References

[1] Gupte S, Mohandas PIT, Conrad JM. 2012. A survey of quadrotor unmanned aerial vehicles. *2012 Proceedings of IEEE Southeastcon, Orlando, FL, USA, 15–18 March 2012*. New York, NY: IEEE. pp. 1–6 doi: 10.1109/SECon.2012.6196930

[2] Ward TA, Fearday CJ, Salami E, Soin NB. 2017. A bibliometric review of progress in micro air vehicle research. *International Journal of Micro Air Vehicles* 9(2):146–165

[3] Mubdir B, Prempain E. 2025. Distributed nonlinear model predictive control for a quadrotor UAV. *International Journal of Micro Air Vehicles* 17:1–18

[4] Dhiman KK, Kothari M, Abhishek A. 2020. Autonomous load control and transportation using multiple quadrotors. *Journal of Aerospace Information Systems* 17(8):417–435

[5] Saska M, Vonásek V, Chudoba J, Thomas J, Loianno G, et al. 2016. Swarm distribution and deployment for cooperative surveillance by micro-aerial vehicles. *Journal of Intelligent & Robotic Systems* 84:469–492
[6] Zhen Z, Xing D, Gao C. 2018. Cooperative search-attack mission planning for multi-UAV based on intelligent self-organized algorithm. *Aerospace Science and Technology* 76:402–411
[7] Lewis MA, Tan KH. 1997. High precision formation control of mobile robots using virtual structures. *Autonomous Robots* 4:387–403
[8] Li NHM, Liu HHT. Formation UAV flight control using virtual structure and motion synchronization. In *2008 American Control Conference, Seattle, WA, USA, 11–13 June, 2008*. New York, NY: IEEE. pp. 1782–1787 doi: 10.1109/ACC.2008.4586750
[9] Askari A, Mortazavi M, Talebi H. 2015. UAV formation control *via* the virtual structure approach. *Journal of Aerospace Engineering* 28(1):04014047
[10] Balch T, Arkin RC. 1998. Behavior-based formation control for multirobot teams. *IEEE Transactions on Robotics and Automation* 14(6):926–939
[11] Lawton JRT, Beard RW, Young BJ. 2003. A decentralized approach to formation maneuvers. *IEEE Transactions on Robotics and Automation* 19(6):933–941
[12] Kim S, Kim Y. 2007. Three dimensional optimum controller for multiple UAV formation flight using behavior-based decentralized approach. *2007 International Conference on Control, Automation and Systems, Seoul, Korea (South), 17–20 October 2007*. New York, NY: IEEE. pp. 1387–1392 doi: 10.1109/ICCAS.2007.4406555
[13] Wang X, Li S, Yu X, Yang J. 2017. Distributed active anti-disturbance consensus for leader-follower higher-order multi-agent systems with mismatched disturbances. *IEEE Transactions on Automatic Control* 62(11):5795–5801
[14] Wang X, Wang G, Li S. 2020. Distributed finite-time optimization for integrator chain multiagent systems with disturbances. *IEEE Transactions on Automatic Control* 65(12):5296–5311
[15] Li G, Wang X, Li S. 2020. Consensus control of higher-order Lipschitz non-linear multi-agent systems based on backstepping method. *IET Control Theory & Applications* 14(3):490–498
[16] Belkacem K, Munawar K, Muhammad SS. 2020. Distributed cooperative control of autonomous multi-agent UAV systems using smooth control. *Journal of Systems Engineering and Electronics* 31(6):1297–1307
[17] Zhang J, Yan J, Zhang P. 2020. Multi-UAV formation control based on a novel back-stepping approach. *IEEE Transactions on Vehicular Technology* 69(3):2437–2448
[18] Ollervides-Vazquez EJ, Rojo-Rodriguez EG, Garcia-Salazar O, Amezquita-Brooks L, Castillo P, et al. 2020. A sectorial fuzzy consensus algorithm for the formation flight of multiple quadrotor unmanned aerial vehicles. *International Journal of Micro Air Vehicles* 12:1–24
[19] Miao Z, Zhong H, Lin J, Wang Y, Fierro R. 2022. Geometric formation tracking of quadrotor UAVs using pose-only measurements. *IEEE Transactions on Circuits and Systems II: Express Briefs* 69(3):1159–1163
[20] Wang X, Xu Y, Cao Y, Li S. 2024. A hierarchical design framework for distributed control of multi-agent systems. *Automatica* 160:111402
[21] Wang X, Wang J, Chen YY, Ma Y, Li S. 2026. Hierarchical consensus of constrained second-order multiagent systems with application to formation of multiple mobile robots. *IEEE Transactions on Automatic Control* 71(2):886–901
[22] Hart PE, Nilsson NJ, Raphael B. 1968. A formal basis for the heuristic determination of minimum cost paths. *IEEE Transactions on Systems Science and Cybernetics* 4(2):100–107
[23] Han W-G, Baek S-M, Kuc T-Y. 1997. Genetic algorithm based path planning and dynamic obstacle avoidance of mobile robots. *1997 IEEE International Conference on Systems, Man, and Cybernetics. Computational Cybernetics and Simulation, Orlando, FL, USA, 12–15 October, 1997*. Vol. 3. New York, NY: IEEE. pp. 2747–2751 doi: 10.1109/ICSMC.1997.635354
[24] Zhao Y, Zheng Z, Zhang X, Liu Y. 2017. Q learning algorithm based UAV path learning and obstacle avoidence approach. *2017 36th Chinese Control Conference (CCC), Dalian, China, 26–28 July 2017*. New York, NY: IEEE. pp. 3397–3402 doi: 10.23919/ChiCC.2017.8027884
[25] Khatib O. 1986. Real-time obstacle avoidance for manipulators and mobile robots. *The International Journal of Robotics Research* 5(1):90–98
[26] González-Sierra J, Hernández-Martínez EG, Ramírez-Neria M, Fernandez-Anaya G. 2023. Smooth collision avoidance for the formation control of first order multi-agent systems. *Robotics and Autonomous Systems* 165:104433
[27] Li B, Gong W, Yang Y, Xiao B. 2023. Distributed fixed-time leader-following formation control for multiquadrotors with prescribed performance and collision avoidance. *IEEE Transactions on Aerospace and Electronic Systems* 59(5):7281–7294
[28] Wang G, Wang X, Li S. 2026. A hierarchical nested constraint scheme for finite-time formation tracking control of disturbed second-order multiagent systems. *IEEE Transactions on Industrial Informatics* 22(1):452–462
[29] Warren CW. Global path planning using artificial potential fields. *Proceedings, 1989 International Conference on Robotics and Automation, Scottsdale, AZ, USA, 14–19 May 1989*. Vol. 1. New York, USA: IEEE. pp. 316–321 doi: 10.1109/ROBOT.1989.100007
[30] Su Y-H, Bhowmick P, Lanzon A. 2024. A fixed-time formation-containment control scheme for multi-agent systems with motion planning: applications to quadcopter UAVs. *IEEE Transactions on Vehicular Technology* 73(7):9495–9507
[31] Qian Z, Chen R, Yi C, Zhai X, Chen B. 2025. Collision avoidance control for autonomous driving with multiple dynamic obstacles in IoV: a prediction-enhanced APF-based approach. *IEEE Internet of Things Journal* 12(13):24968–24984
[32] Matoui F, Boussaid B, Metoui B, Abdelkrim MN. 2020. Contribution to the path planning of a multi-robot system: centralized architecture. *Intelligent Service Robotics* 13(1):147–158
[33] Hu J, Wang M, Zhao C, Pan Q, Du C. 2020. Formation control and collision avoidance for multi-UAV systems based on Voronoi partition. *Science China Technological Sciences* 63:65–72
[34] Pan Z, Zhang C, Xia Y, Xiong H, Shao X. 2022. An improved artificial potential field method for path planning and formation control of the multi-UAV systems. *IEEE Transactions on Circuits and Systems II: Express Briefs* 69(3):1129–1133
[35] Huang T, Huang D, Qin N, Li Y. 2021. Path planning and control of a quadrotor UAV based on an improved APF using parallel search. *International Journal of Aerospace Engineering* 2021(1):5524841
[36] Wang L, Zhu D, Pang W, Luo CM. 2023. A novel obstacle avoidance consensus control for multi-AUV formation system. *IEEE/CAA Journal of Automatica Sinica* 10(5):1304–1318
[37] Liu H, Li B, Ahn CK. 2025. Asymptotically stable-learning-based formation control for multiquadrotor UAVs. *IEEE Internet of Things Journal* 12(13):24985–24995
[38] Hong Y, Hu J, Gao L. 2006. Tracking control for multi-agent consensus with an active leader and variable topology. *Automatica* 42(7):1177–1182
[39] Krstic M, Kanellakopoulos I, Kokotovic PV. 1995. *Nonlinear and adaptive control design*. USA: John Wiley & Sons, Inc.
[40] Khalil HK. 2002. *Nonlinear systems*. 3rd Edition. Upper Saddle River, NJ: Prentice Hall.
[41] Bitcraze: Crazyflie 2.1. www.bitcraze.io

Copyright: © 2026 by the author(s). Published by Maximum Academic Press, Fayetteville, GA. This article is an open access article distributed under Creative Commons Attribution License (CC BY 4.0), visit https://creativecommons.org/licenses/by/4.0/.